

Received April 10, 2018, accepted May 9, 2018, date of publication May 16, 2018, date of current version June 5, 2018.

Digital Object Identifier 10.1109/ACCESS.2018.2836329

Capacitively Coupled Resistivity Imaging for Biomaterial and Biomedical Applications

YANDAN JIANG^{1, 2} AND MANUCHEHR SOLEIMANI¹

¹Engineering Tomography Laboratory, Department of Electronic and Electrical Engineering, University of Bath, Bath BA2 7AY, U.K.

²State Key Laboratory of Industrial Control Technology, College of Control Science and Engineering, Zhejiang University, Hangzhou 310027, China

Corresponding author: Yandan Jiang (jiangyandan123@163.com)

This work was supported by the China Scholarship Council under Grant 201706320268.

ABSTRACT Imaging of electrical conductivity is a promising technique in biomedical field, which can reveal the impedance distribution within the region of interest. However, the contact measurement of traditional electrical impedance tomography (EIT) results in some challenging practical limitations on its applications. This paper introduces a novel capacitively coupled EIT to the biomaterial/biomedical field for resistivity imaging, and studies various aspects of this new contactless technique on practical applications. A 12-electrode experimental phantom is developed and the corresponding computational model is established to obtain the sensitivity matrix of the phantom. A hybrid image reconstruction method, which combines the Tikhonov regularization method and the simultaneous iterative reconstruction technique, is introduced to solve the inverse problem. In biomedical applications, the frequency-dependent conductivity aspect is very critical. Therefore, both the time-difference and frequency-difference imaging methods are investigated. A background calibration approach is proposed for the frequency-difference capacitively coupled EIT to overcome the frequency dependence of the background signal. Experiments were carried out with three kinds of biomaterials and three backgrounds with different conductivities. Results show the working principles and potential of the capacitively coupled EIT on biomaterial and biomedical applications.

INDEX TERMS Electrical impedance tomography (EIT), capacitively coupled EIT, biomaterial and biomedical application, time-difference imaging, frequency-difference imaging.

I. INTRODUCTION

Electrical impedance tomography (EIT) is a non-invasive technique that can implement imaging of the impedance distribution within a volume, either a part of human body in biomedical application or the contents of a pipeline/vessel in process application [1]–[5]. Since the first EIT system was developed in 1983 by Barber *et al.* [6], this technique has drawn much attention from researchers and an intensive development of EIT has taken place in the biomedical field. Then, in late 1980s, impedance tomography was introduced into process tomography and a particular case of EIT termed electrical resistance tomography (ERT) was invented, which reconstructed the resistivity/conductivity distribution of the sensing area [4], [7]. EIT has many advantages and the major ones are low cost, rapid response and no radiation hazard, which makes it a promising technique and worth investigating.

However, according to the contact conductivity measurement principle, the electrodes of EIT should be in direct

contact with the conductive medium, which certainly have some major negative influences on measurement [8], [9]. In the medical/biomedical imaging field, one major problem of this contact measurement approach is that the electrode-skin contact impedance between the electrodes and the human body (or biological specimen) will be included in the measurements [10]–[13]. This contact impedance is usually high and quite variable due to body surface condition and body movement. Besides, research results show that this contact impedance is sensitive to properties of the contact layer, while in practical clinical experiments one usually lacks priori knowledge of the boundary properties. So, the contact impedance is a crucial accuracy-limiting factor. During the past decades, many research works have been undertaken to seek effective ways to reduce or estimate the unknown contact impedances. In 1993, Brown [1] used large electrodes to provide a more uniform current distribution and reduce the contact impedance, and used the finite element method (FEM) to model the contact impedance. In 2002, Vilhunen *et al.* [14]

and Heikkinen *et al.* [15] proposed an approach for estimating the contact impedance of the electrodes simultaneously with the estimation of the admittivity of the object. The complete electrode model (CEM) without any geometrical constraints was used in the estimation procedure. In 2008, Kolehmainen *et al.* [11] proposed a novel image reconstruction method in which the systematic errors induced by inaccurately known boundary and contact impedances were eliminated as part of the image reconstruction. In 2011, Demidenko *et al.* [16] developed a new fast and reliable gapZ method for the simultaneous estimation of contact impedances and conductivity on the 2-D homogeneous disk using the magic Toeplitz matrix. In 2012, Cardu *et al.* [12] studied the dependence of the contact impedance on geometrical factors and found that flat electrodes were sensitive to changes in the outer skin layer properties related to hydration and thickness, while spike electrodes were not. In practical sense the contact impedance is still a major limiting factor in medical EIT.

It is important to keep interaction and develop EIT along similar lines in both biomedical and process tomography fields because they may suffer from similar problems, and the development in one can provide reference for the other [1], [17]. As for process tomography fields, like the multi-phase flow field, direct contact between EIT electrodes and fluid also results in bad sides (electrochemical erosion effect, polarization effect and contamination of the electrodes), leading to unpredictable measurement errors in the long run [7], [18]. So, at the same time, researchers also made efforts to overcome these drawbacks [19]–[21]. In 2010, Brown *et al.* [2] used a typical electrical capacitance tomography (ECT) sensor to capture the information of the conductivity distributions inside a pipe and got good results in both position and size. Also in 2010, Wang *et al.* [21]–[23] proposed the capacitively coupled electrical resistance tomography (CCERT) to implement contactless imaging of conductivity distribution based on the capacitively coupled contactless conductivity detection (C^4D) technique and then developed a specified CCERT system for real-time measurement, which provided reference for other research works as a new approach to overcome the drawbacks of contact measurement.

By referring to the CCERT in process tomography, this paper aims to study for the first time the feasibility of this novel capacitively coupled EIT technique on biomaterial/biomedical applications to overcome the contact impedance problem of traditional EIT. Time-difference imaging at different frequencies is studied and the feasibility of contactlessly analyzing the frequency-dependence characteristics of the tested biomaterials (i.e. the relationship between the conductivity of biomaterial anomaly and the excitation frequency) is verified. Besides, frequency-difference imaging of capacitively coupled EIT is also investigated. Frequency dependent conductivity of biological samples is a major difference with the objects in industrial/process applications, offering good opportunities for applications when a reference

data may not be available for the same subject. Methods concerning the measurement principle, the forward problem and the inverse problem of this work are described in Section II. Image reconstruction results of several biomaterial samples are presented in Section III.

II. METHODS

A. MEASUREMENT PRINCIPLE

1) PHANTOM

A 12-electrode capacitively coupled EIT phantom is developed in this work. Fig. 1(a) shows the construction of the phantom, with 12 electrodes mounted equidistantly on the outer periphery of the insulation pipe. When the pipe is filled with conductive medium, for any two electrodes, the electrode, the insulation pipe and the conductive medium form two coupling capacitances [22], [23]. The impedance model of biological tissues can be modeled as a group of electronic components. One of the simplest employs just three components [24], as shown in Fig. 1(b). The extracellular space of the biological tissue is represented as a resistor (R_e), and the intracellular space and the membrane are modeled respectively as a resistor (R_i) and a capacitor (C_m). Both the extracellular and intracellular spaces are conductive, while the lipid membrane is an insulator. For biomedical applications, the conductive medium inside the sensing area is just the same as that in biological tissues (both includes extracellular and intracellular conductive spaces, and insulation membrane), which means the impedance model inside the sensing area is equivalent to the impedance model of biological tissues. So, the equivalent circuit between any electrode pair can be simplified as two coupling capacitances in series with the impedance of the biological tissue, as shown in Fig. 1(c). C_1 is the coupling capacitance formed by electrode *a*, the insulation pipe and the conductive medium, and C_2 is that formed by electrode *b*, the insulation pipe and the conductive medium. R_i and C_m are respectively the equivalent resistance of the intracellular space and the equivalent capacitance of the membrane of the biological tissue between electrode *a* and *b*.

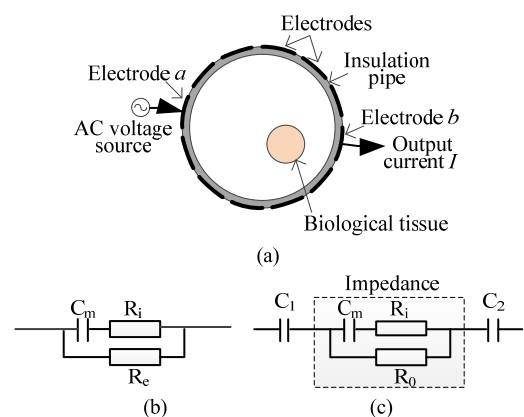


FIGURE 1. The capacitively coupled EIT phantom. (a) Construction. (b) Impedance model of biological tissues. (c) Equivalent circuit of an electrode pair.

R is the equivalent resistance of the conductive background and the extracellular space of the biological tissue. When the AC voltage source is applied to the excitation electrode, a current I which reflects the impedance of the sensing area can be obtained from the detection electrode. In a measurement cycle, electrode 1 is first selected as the excitation electrode and electrode 2~12 are selected one by one as the detection electrode. Then, electrode 2 is to be the excitation electrode and electrode 3~12 are selected by turn to be the detection electrode. Go on until electrode 11 and electrode 12 are selected as the measurement pair. So, there are 66 independent measurements for this 12-electrode phantom in a measurement cycle. In this work, only the resistance information (real part of the current measurement) which reflects the conductivity/resistivity information of the sensing area is used for imaging.

2) TIME-DIFFERENCE IMAGING

Compared with absolute/static imaging, difference imaging effectively deals with the uncertainty of the conductivity distribution and cancels common errors by taking a reference measurement and imaging the variation in conductivity distribution, so it is restricted to dynamic phenomena [25].

As shown in Fig. 2, time-difference means two measurements are obtained at different times: one is taken as a reference when the phantom is full of homogeneous conductive background and the other is taken when the anomaly/object is introduced into the phantom [17]. Then, the conductivity change between the two measurements is reconstructed as an image. So far, time-difference imaging is widely applied to both biomedical and industrial applications.

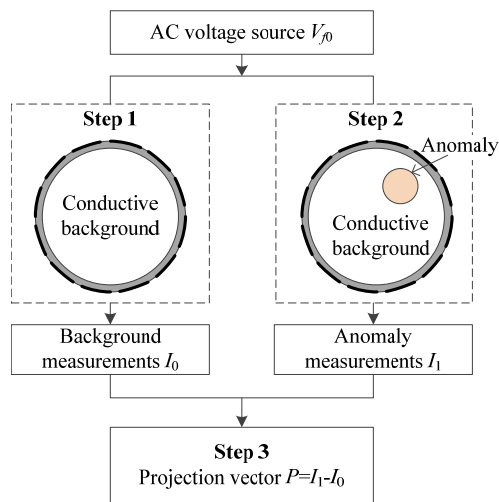


FIGURE 2. Measurement principle of time-difference imaging.

3) FREQUENCY-DIFFERENCE IMAGING

In medical imaging field, there are cases where time-referenced data are not available and the application of time-difference imaging is difficult [25]–[27]. To solve this problem, some medical researchers attempted to use measurements between different frequencies instead of

different times, based on the observation that the complex conductivity spectra of numerous biological tissues show frequency-dependent changes [17]. That’s how frequency-difference/multi-frequency imaging showed up.

Fig. 3 shows the measurement principle of frequency-difference imaging with measurements obtained at two frequencies. Frequency-difference imaging obtains boundary measurements under at least two frequencies and reconstructs the image of conductivity change in the sensing area utilizing measurement differences between chosen frequencies. Different materials have different conductivity spectra, so one material can be distinguished from the other by frequency-difference imaging.

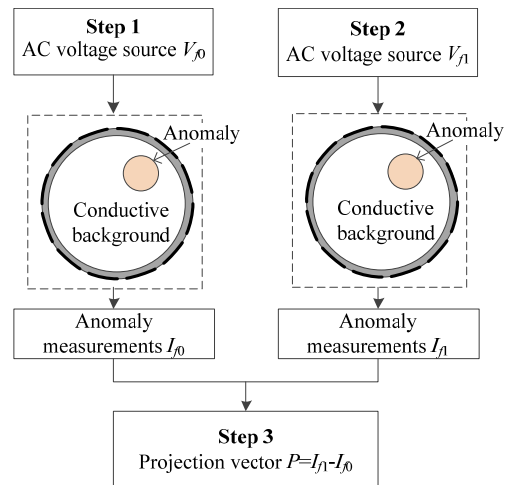


FIGURE 3. Measurement principle of frequency-difference imaging.

B. THE FORWARD PROBLEM

1) MODEL OF THE PHANTOM

In most electrical impedance tomography applications, the frequency of the excitation electrical signal is below 1 MHz, so the corresponding wavelength is much larger than the phantom size. That means the sensing region of the phantom in Fig. 1 can be regarded as a quasi-static electromagnetic field and the coupling effect between electric field and magnetic field can be neglected. Besides, to simplify the model, the fringe effect caused by the finite electrode length is neglected. Thus, according to Maxwell’s equations, the sensing region Ω of the phantom can be modeled as [22]

$$\nabla \cdot ((\sigma(x, y) + j\omega\varepsilon(x, y))\nabla\phi(x, y)) = 0 \quad (x, y) \subseteq \Omega \quad (1)$$

where, $\sigma(x, y)$, $\varepsilon(x, y)$ and $\phi(x, y)$ are the spatial conductivity, permittivity and potential distributions. $\omega=2\pi f$ is the angular frequency of the excitation AC voltage source, f is the frequency of the AC voltage source.

Then the boundary conditions are defined as

$$\begin{cases} \phi_a(x, y) = V & (x, y) \subseteq \Gamma_a \\ \phi_b(x, y) = 0 & (x, y) \subseteq \Gamma_b \\ \partial\phi_c(x, y)/\partial\vec{n} = 0 & (x, y) \subseteq \Gamma_c, (c \neq a, b) \end{cases} \quad (2)$$

where, V is the amplitude of the excitation AC voltage source. $\Gamma_1, \Gamma_2, \Gamma_3, \dots, \Gamma_{12}$ represent the spatial locations of the 12 electrodes. \vec{n} denotes the outward unit normal vector. a, b and c are the indexes of the excitation electrode, the detection electrode and the floating electrode, respectively.

2) SENSITIVITY MATRIX

Based on the established mathematical model and FEM [28], [29], simulation work was undertaken by COMSOL Multiphysics and MATLAB to obtain the sensitivity matrix of the phantom. The sensing area of the phantom was meshed into 864 triangle elements. The excitation frequency and the amplitude of the excitation voltage source were 500 kHz and 1 V. The conductivities of the background and the anomaly were set to $\sigma_0=0.043$ S/m and $\sigma_1=0.1$ S/m, respectively. After applying the AC voltage signal to the excitation electrode, the i th current measurement can be obtained on the detection electrode according to (3).

$$I_i = \int_{\Gamma_b} J_{a-b} d\Gamma_b \quad (3)$$

where, $a-b$ is the i th measurement electrode pair, $i = 1, 2, \dots, m$ ($m = 66$). J_{a-b} is the current density measured on the detection electrode b and Γ_b is the surface area of the detection electrode. Then the resistance R_i of the measured fluid between the two electrodes is

$$R_i = \text{Re}(1/I_i) \quad (4)$$

In a measurement cycle, 66 electrode pairs will be selected to obtain 66 independent measurements. The sensitivity matrix is

$$S = [s_{ij}] \quad (5)$$

where, s_{ij} is the sensitivity of the j th element under the i th electrode pair (i.e. the i th independent measurement), $j = 1, 2, \dots, n$. s_{ij} is defined as

$$s_{ij} = \frac{\partial I}{\partial \sigma} = \frac{\text{Re}(I_i^j - I_i^0)}{\sigma_1 - \sigma_0} = \frac{1/R_i^j - 1/R_i^0}{\sigma_1 - \sigma_0} \quad (6)$$

where, I_i^0 and R_i^0 represent the i th current measurement and the corresponding resistance when the pipe is full of conductive background ($\sigma = \sigma_0$). I_i^j and R_i^j are the i th current measurement and the corresponding resistance when the conductivity of the j th element changes from σ_0 to σ_1 and the remaining elements are still kept at σ_0 .

C. THE INVERSE PROBLEM

The task of image reconstruction in EIT is to determine the gray vector G in the region of interest based on the measured projection vector P and the pre-determined sensitivity matrix S . This can be implemented by solving the following equation [30]–[32]

$$P = SG \quad (7)$$

where, $P=[p_i]$ is the projection vector calculated by measurements, $S=[s_{ij}]$ is the sensitivity matrix and $G=[g_j]$ is the

gray vector of the elements which reflects the conductivity distribution of the sensing area.

It is difficult to solve the inverse problem in (7). First, the solution is not unique because the number of variables (the number of elements) is bigger than the number of equations (the number of projections). Second, the problem is ill-posed, which means the solution G is sensitive to small perturbations of the projection P . Besides, the EIT is a so-called soft-field tomography, i.e. the true sensitivity matrix varies with the actual conductivity distribution. After decades of research, both non-iterative and iterative image reconstruction algorithms have been proposed and studied to solve the inverse problem [30]–[41].

In this work, the inverse problem is implemented by a hybrid image reconstruction algorithm, which is the combination of Tikhonov regularization and SIRT algorithm. The Tikhonov regularization is used to obtain an approximate stable solution (an initial denoised image) and then the SIRT algorithm is used to obtain the final reconstructed image by standard iteration [34]. The performance of this hybrid algorithm in electrical tomography have been tested and compared in [34] and [35]. Experimental results show that this hybrid algorithm can obtain higher quality images than traditional methods like filtered linear back-projection, Tikhonov regularization and projected Landweber iteration. Besides, research results in [34] also indicated that this hybrid algorithm is more suitable for capacitively coupled electrical resistance tomography.

Tikhonov regularization is one of the most commonly used methods of solving ill-posed inverse problem and has been applied to EIT for image reconstruction. It is a one-step method that introduces a trade-off between actually getting a solution to the problem and not letting the solution $\|G\|$ getting too big [31]. So, the general form of the objective function in Tikhonov regularization is [36], [37], [41]

$$G_\lambda = \arg \min_G \|SG - P\|^2 + \lambda^2 \|G\|^2 \quad (8)$$

where, λ is the regularization parameter that controls the amount of regularization. The solution can be obtained by solving the following equation:

$$\frac{\partial F(G)}{\partial G} = 2S^T(SG - P) + 2\lambda^2 G = 0 \quad (9)$$

where, $F(G) = \|SG - P\|^2 + \lambda^2 \|G\|^2$, so the solution G_λ can be described as

$$G_\lambda = (S^T S + \lambda^2 I_n)^{-1} S^T P \quad (10)$$

where, I_n is the identity matrix.

The regularization parameter λ in this work is pre-determined by the L-curve method. Different λ leads to different regularized solutions in (10). L-curve is a log-log plot of the norm of the regularized solution versus the norm of the corresponding residual [41]–[43]. According to the L-curves of several tested data groups, setting the value of λ^2 between $1e-3$ to $5e-2$ can provide better image reconstruction quality. So, the value of λ^2 is set to $5e-3$.

Simultaneous iterative reconstruction technique (SIRT) is a commonly used method for image reconstruction in computerized tomography and has been introduced to EIT as an effective iterative method [31]–[33], [39]. During iteration, SIRT calculates an average correction value for every pixel/element in the sensing area based on all the related projections, so it can reduce noises and get a smooth image. Finally, SIRT can determine an optimal solution which is the closet one to the actual solution. The detailed SIRT algorithm is described as following.

More detailed information concerning the hybrid algorithm and its performance are available in [34] and [35].

III. RESULTS

A. EXPERIMENTS

Experiments were carried out with a 12-electrode capacitively coupled EIT phantom. The electrode angle and the electrode length of the phantom were 24° and 150 mm. The inner and outer diameters of the phantom were 102 mm and 110 mm, respectively. An impedance analyzer (Keysight 4990A) was used to obtain resistance measurements. The amplitude of the excitation voltage of the impedance analyzer was set to 1 V. The sweep frequency range was set from 10 kHz to 1 MHz. Performing a new type of the EIT directly on the patient’s body is neither ethical nor permitted, hence many researchers undertook initial biomedical-related research works with phantoms and biomaterial samples [25]–[27], [44]–[46]. So, in this work, experimental materials were tap water and saline (as backgrounds with different conductivities), and three biomaterial samples (as anomalies: potato, carrot and cucumber). The conductivity of the background inside the phantom was measured by the Jenway 4510 conductivity meter. The experimental temperature in the laboratory is stable during the experiments which is about 25°C. Fig. 4 shows a photo of the phantom.

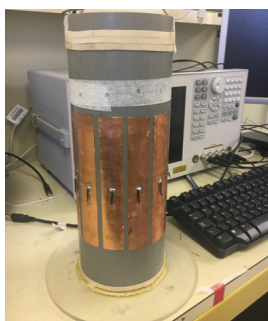


FIGURE 4. Photo of the 12-electrode capacitively coupled EIT phantom.

B. TIME-DIFFERENCE IMAGING RESULTS

1) IMAGE RECONSTRUCTION RESULTS

Table 2 shows the time-difference imaging results obtained at frequencies of 300 kHz, 600 kHz and 900 kHz. The actual position and size of the anomaly is represented by a circle in red edge. As can be seen from the table, as the conductivity of

TABLE 1. SIRT algorithm.

Algorithm: SIRT

Input:

Given actual projection vector $P = [p_i], i = 1, 2, \dots, m$,
 initial gray vector $G^1 = [g_j^1], j = 1, 2, \dots, n$,
 sensitivity matrix $S = [s_{ij}], i = 1, 2, \dots, m, j = 1, 2, \dots, n$,
 scalars $\varepsilon > 0$ and $\xi > 0$.
 Set iteration index $l=1, c_r = 1$.

Define contribution index $N_{ij} = \begin{cases} 1, & s_{ij} \geq \xi \\ 0, & s_{ij} < \xi \end{cases}$

while $c_r > \varepsilon$ do

for $i = 1, 2, \dots, m$ do

Calculate estimated projection $\hat{p}_i = \sum_{j=1}^n s_{ij} g_j^l$

Calculate projection deviation $\Delta p_i = p_i - \hat{p}_i$

Calculate pixel correction matrix $C^l = [c_{ij}^l]$

$$c_{ij}^l = \begin{cases} \Delta p_i s_{ij} / \sum_{j=1}^n (s_{ij})^2, & N_{ij} = 1 \\ 0, & N_{ij} = 0 \end{cases}$$

end for

for $j = 1, 2, \dots, n$ do

Calculate average pixel correction value

$$\Delta g_j^l = (\sum_{i=1}^m c_{ij}^l) / (\sum_{i=1}^m N_{ij})$$

Update gray vector $G^{l+1} = [g_j^{l+1}], g_j^{l+1} = g_j^l + \Delta g_j^l$

end for

Let $c_r = \max \{ |\Delta g_1^l|, |\Delta g_2^l|, \dots, |\Delta g_n^l| \}$

$l = l+1$

end while

Output: g_j^l

background increases, the difficulty of imaging also increases because the conductivity difference between the background and the anomaly narrows. Another obvious point is that the increase of excitation frequency can reduce the imaging difficulty because of the frequency-dependence of the biomaterial anomaly.

2) FREQUENCY-DEPENDENCE OF BIOMATERIALS

With the time-difference images, the frequency-dependence characteristics of biomaterials are analyzed. For time-difference imaging, the conductivity difference between the background and the anomaly is imaged, so the obtained gray vector represents the relative conductivity distribution of the sensing area as relative to the conductivity of the background.

To investigate the relationship between the conductivity of biomaterials with the excitation frequency, the average relative conductivity of the anomaly is calculated, which is defined as

$$g_a = \frac{1}{N_a} \sum_{j=1}^n r_j g_j^* \quad (11)$$

TABLE 2. Time-difference imaging results of capacitively coupled EIT.

Anomaly	Background	300kHz	600kHz	900kHz
Potato	Tap water ($\sigma_0=0.043$ S/m)			
	Saline ($\sigma_0=0.068$ S/m)			
	Saline ($\sigma_0=0.096$ S/m)			
Carrot	Tap water ($\sigma_0=0.043$ S/m)			
	Saline ($\sigma_0=0.068$ S/m)			
	Saline ($\sigma_0=0.096$ S/m)			
Cucumber	Tap water ($\sigma_0=0.043$ S/m)			
	Saline ($\sigma_0=0.068$ S/m)			
	Saline ($\sigma_0=0.096$ S/m)			

where, N_a is the number of elements/pixels inside the anomaly area. g_j^* and r_j is the gray value and effectiveness coefficient of the j th element. r_j is defined as

$$r_j = \begin{cases} 1, & e_j \in \Omega_a \\ 0, & e_j \notin \Omega_a \end{cases} \quad (12)$$

where, e_j is the geometry of the j th element and Ω_a represents the anomaly geometry.

In this work, the relationship between the average relative conductivity of different biomaterials and the excitation frequency is studied. The investigated frequency ranges from 200 kHz to 1 MHz. Fig. 5 shows the frequency-dependence characteristics of the three biomaterial samples respectively inside the same background (BG), which indicates that the conductivities of all the three samples have a positive correlated relationship with the excitation frequency (i.e. As the frequency increases, the relative conductivity of the sample goes up as well). The figure also shows that the potato sample has a higher conductivity than the carrot sample, and the cucumber sample has the lowest conductivity among the three biomaterials. According to [27] and [44], the frequency-dependence characteristics of the three biomaterial samples shown in Fig. 5, i.e. the frequency-conductivity changing trend and the difference between different samples, are in accordance with the actual properties of the three bio-samples within the tested frequency range.

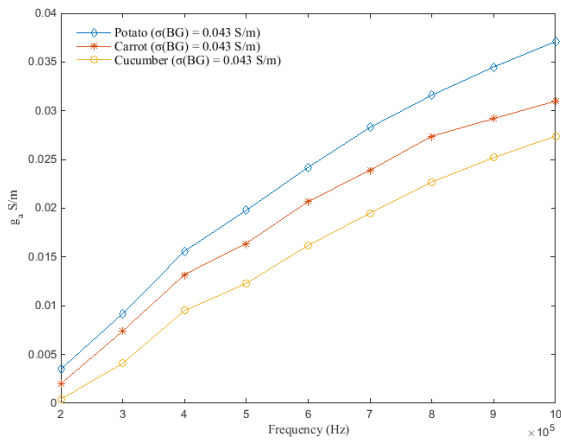


FIGURE 5. Frequency-dependence characteristics of three biomaterial samples (potato, carrot and cucumber): the relationship between the average relative conductivity of the sample inside the background with the conductivity of 0.043 S/m and the excitation frequency.

In addition, the relationship between the average relative conductivity of a specified biomaterial inside different backgrounds and the excitation frequency is also investigated. Fig. 6 shows the frequency-dependence characteristics of a carrot sample inside three different backgrounds with the conductivity of 0.043 S/m, 0.068 S/m and 0.096 S/m, respectively. It is shown that as the conductivity of the background becomes higher, the relative conductivity of the sample gets lower. Besides, the change of the background conductivity

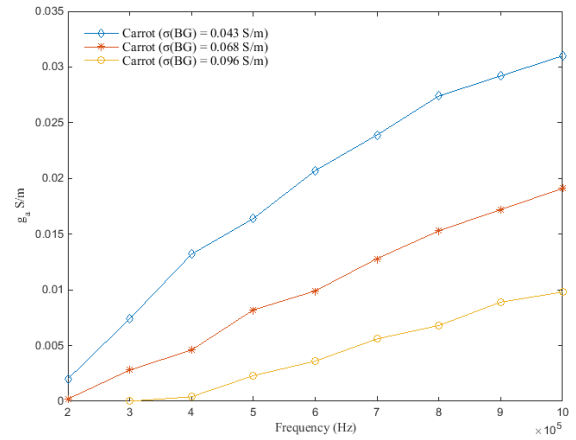


FIGURE 6. The frequency-dependence characteristics of a carrot sample inside three different backgrounds with the conductivity of 0.043 S/m, 0.068 S/m and 0.096 S/m respectively.

has no significant influence on the frequency-dependence trend of the biomaterial.

C. FREQUENCY-DIFFERENCE IMAGING RESULTS

1) TRADITIONAL FREQUENCY-DIFFERENCE IMAGING

As mentioned in Section II, in frequency-difference imaging, the difference of measurements obtained at different frequencies is utilized as the projection vector, so the measurements with only the background is not needed. The frequency-difference imaging results in Table 3 shows that the traditional frequency-difference imaging technique is not feasible for the capacitively coupled EIT phantom.

TABLE 3. Traditional frequency-difference imaging results.

Anomaly	Background	200k-500k	200k-800k
Potato	Tap water ($\sigma_0=0.043$ S/m)		
	Saline ($\sigma_0=0.068$ S/m)		

Finding the problem is always the key of seeking for an effective solution, so going back to the measurements may provide some reference.

Fig. 7 shows the background current measurements (Fig. 7(a)) and the anomaly current measurements with a potato inside the phantom (Fig. 7(b)) at three different frequencies of 200 kHz, 500 kHz and 800 kHz. It can be found that although there is only background (no biomaterial anomaly in the phantom), the measurements change with the frequency, which may be the problem.

Fig. 8 shows the difference between current measurements obtained at frequency of 200 kHz and those obtained

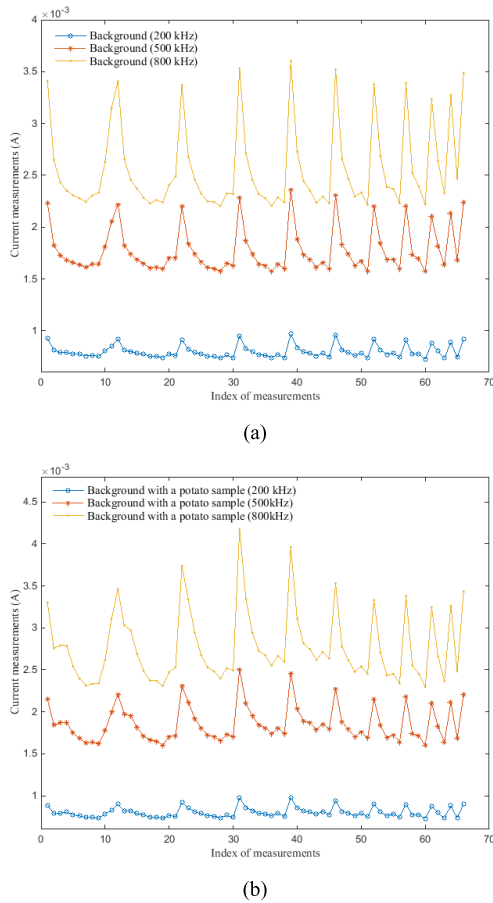


FIGURE 7. Current measurements obtained at three different frequencies: 200 kHz, 500 kHz and 800 kHz, respectively. (a) Background measurements. (b) Anomaly measurements (with a potato sample inside the background).

at 500 kHz (i.e. the projections of frequency-difference imaging in Fig. 3), for both the background measurements and the anomaly measurements (with a potato inside the background). Whether the biomaterial anomaly is inside the phantom or not, when the frequency changes, the current measurements change by almost the same level and in the same trend. That means the frequency-dependence of the background signal of the capacitively coupled EIT, including the pipe wall and the conductive medium, outweighs the frequency-dependence of the biomaterial anomaly. In other words, as the frequency changes, the change of background conductivity covers the change of anomaly conductivity.

2) FEASIBILITY OF BACKGROUND CALIBRATION

Considering calibrating the frequency-dependence of the background by replacing the projection vector in Fig. 3 with the following equation:

$$P = (I_{f_1} - I_{f_0}) - (I_{f_1}^0 - I_{f_0}^0) \tag{13}$$

where, I_{f_1} and I_{f_0} are the anomaly measurement vectors obtained at frequency f_1 and f_0 , and $I_{f_1}^0$ and $I_{f_0}^0$ are the

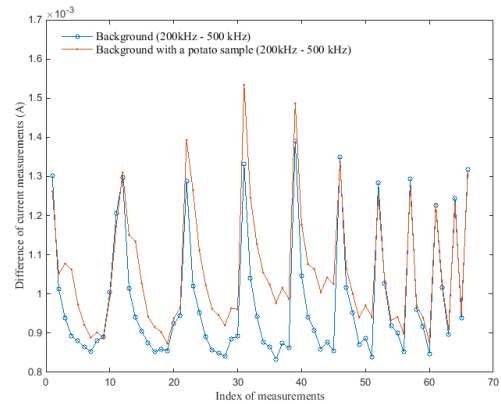


FIGURE 8. Difference between current measurements obtained at 200 kHz and current measurements obtained at 500 kHz.

background measurement vectors obtained at frequency f_1 and f_0 , respectively.

Table 4 shows the frequency-difference imaging results of capacitively coupled EIT with the calibrated projection vector in (13).

IV. DISCUSSION

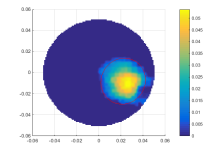
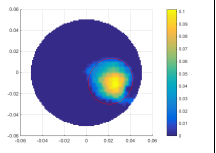
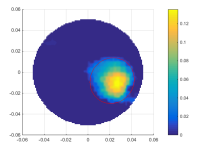
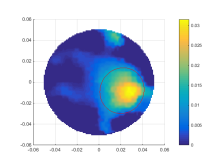
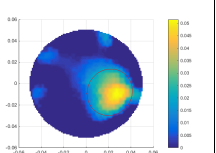
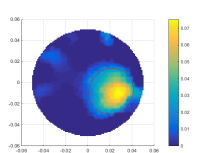
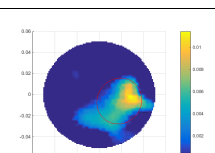
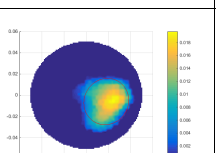
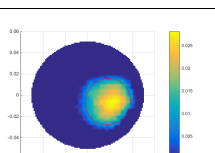
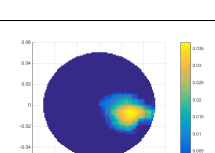
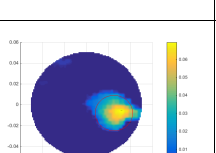
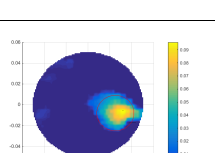
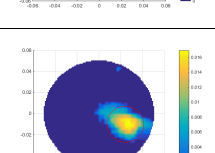
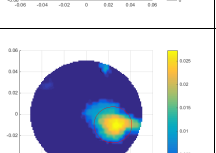
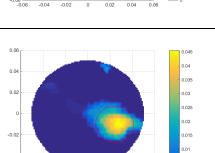
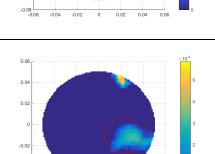
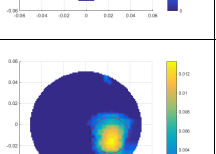
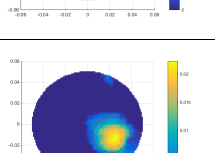
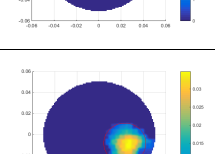
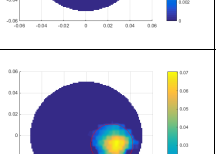
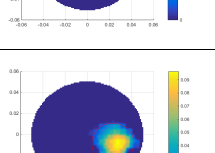
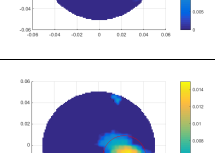
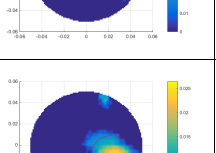
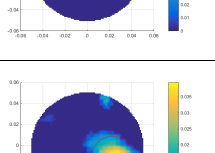
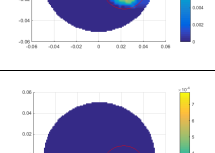
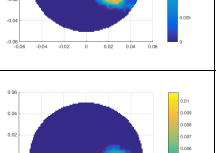
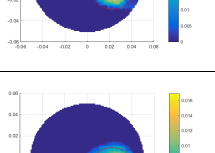
Both the time-difference and frequency-difference imaging results are presented in Section III.

The time-difference imaging results of the capacitively coupled EIT with biomaterial anomalies verify the feasibility of this contactless measurement technique on biomedical applications. Fig. 5 and Fig. 6 indicate the potential of capacitively coupled EIT in studying the frequency-dependence characteristics of biomaterials and the possibility in telling one biomaterial from the other, which is meaningful in medical applications and food industry.

The frequency-difference imaging results indicate that the background, including the pipe wall and the conductive medium inside the pipe, also shows frequency-dependence characteristic, which leads to the failure of direct frequency-difference imaging. Then an approach of background calibration for the capacitively couple EIT is proposed. This approach, like time-difference imaging, requires both the background measurements and the anomaly measurements, but needs measurements under at least two different frequencies. The value of this approach is that better images with more constant size of the anomaly can be reconstructed than time-difference imaging.

The proposed background calibration in (13) requires both the background measurements and the anomaly measurements, which leads back to the problem of time-difference imaging (there are cases where time-referenced/background data are not available). So, further study on seeking for a more general background calibration method which is also suitable for cases where background measurements of the object are not available should be undertaken in the future, either by modeling of the frequency-dependence characteristic of the background or by utilizing a general set of background measurements to calibrate the practical anomaly measurements.

TABLE 4. Frequency-difference imaging results after background calibration.

Anomaly	Background	200 kHz-300 kHz	200 kHz-600 kHz	200 kHz-900kHz
Potato	Tap water ($\sigma_0=0.043$ S/m)			
	Saline ($\sigma_0=0.068$ S/m)			
	Saline ($\sigma_0=0.096$ S/m)			
Carrot	Tap water ($\sigma_0=0.043$ S/m)			
	Saline ($\sigma_0=0.068$ S/m)			
	Saline ($\sigma_0=0.096$ S/m)			
Cucumber	Tap water ($\sigma_0=0.043$ S/m)			
	Saline ($\sigma_0=0.068$ S/m)			
	Saline ($\sigma_0=0.096$ S/m)			

V. CONCLUSION

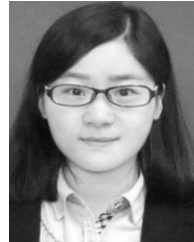
In this work, a novel capacitively coupled EIT is introduced to biomaterial/biomedical application and the feasibility of capacitively coupled resistivity imaging of biomaterials is studied. A 12-electrode capacitively coupled EIT phantom is developed and the corresponding mathematical model is established to solve the forward problem. With the model and FEM, the sensitivity matrix of the phantom is obtained. A hybrid image reconstruction algorithm, which combines the Tikhonov regularization method and the SIRT algorithm, is introduced to solve the inverse problem. Take the frequency dependent conductivity characteristics of biomaterials into consideration, both time-difference imaging and frequency-difference imaging are investigated within a frequency range from 200 kHz to 1 MHz. Experiments were carried out with three backgrounds with different conductivities of 0.043 S/m, 0.068 S/m and 0.096 S/m. And, three kinds of biomaterial samples, potato, carrot and cucumber, were selected as the anomaly. Time-difference imaging results show the feasibility of this contactless technique on biomaterial and biomedical applications, and its potential in analyzing frequency-dependence characteristics of biomaterials. Traditional frequency-difference imaging failed to get valuable images with the capacitively coupled EIT phantom because of an unknown frequency-dependence of the background measurements. Then, a background calibration approach for frequency-dependence capacitively coupled EIT is proposed and acceptable frequency-difference images can be obtained after calibration.

Compared with traditional EIT, this capacitively coupled EIT can implement contactless resistivity imaging, which can overcome the main drawbacks and limitations of traditional EIT in biomaterial/biomedical applications, such as the contamination of electrodes, the contact impedance and body movement. This is very first work introducing the capacitively coupled conductivity measurement technique to the biomaterial/biomedical EIT field using comprehensive sets of experimental test cases the potential clinical impact should be obvious

REFERENCES

- [1] B. H. Brown, "Medical impedance tomography and process impedance tomography: A brief review," *Meas. Sci. Technol.*, vol. 12, no. 8, pp. 991–996, 2001.
- [2] B. H. Brown, "Electrical impedance tomography (EIT): A review," *J. Med. Eng. Technol.*, vol. 27, no. 3, pp. 97–108, 2003.
- [3] R. Harikumar, R. Prabu, and S. Raghavan, "Electrical impedance tomography (EIT) and its medical applications: A review," *Int. J. Soft Comput. Eng.*, vol. 3, no. 4, pp. 193–198, Sep. 2013.
- [4] T. A. York, "Status of electrical tomography in industrial applications," *J. Electron. Imag.*, vol. 10, no. 3, pp. 608–619, 2001.
- [5] K. H. Wei, C.-H. Qiu, and K. Primrose, "Super-sensing technology: Industrial applications and future challenges of electrical tomography," *Philos. Trans. Roy. Soc. A, Math., Phys. Eng. Sci.*, vol. 374, no. 2070, pp. 602–617, 2016.
- [6] D. C. Barber, B. H. Brown, and I. L. Freeston, "Imaging spatial distributions of resistivity using applied potential tomography—APT," in *Information Processing in Medical Imaging*. Dordrecht, The Netherlands: Springer, 1984, pp. 446–462.
- [7] Y. A. Wahab *et al.*, "Non-invasive process tomography in chemical mixtures—A review," *Sens. Actuators B, Chem.*, vol. 210, pp. 602–617, Apr. 2015.
- [8] A. McEwan, G. Cusick, and D. S. Holder, "A review of errors in multi-frequency EIT instrumentation," *Physiol. Meas.*, vol. 28, no. 7, pp. 197–215, 2007.
- [9] M. Soleimani, C. Gómez-Laberge, and A. Adler, "Imaging of conductivity changes and electrode movement in EIT," *Physiol. Meas.*, vol. 27, no. 5, pp. S103–S113, 2006.
- [10] P. Hua, E. J. Woo, J. G. Webster, and W. J. Tompkins, "Finite element modeling of electrode-skin contact impedance in electrical impedance tomography," *IEEE Trans. Biomed. Eng.*, vol. 40, no. 4, pp. 335–343, Apr. 1993.
- [11] V. Kolehmainen, M. Lassas, and P. Ola, "Electrical impedance tomography problem with inaccurately known boundary and contact impedances," *IEEE Trans. Med. Imag.*, vol. 27, no. 10, pp. 1404–1414, Oct. 2008.
- [12] R. Cardu, P. H. W. Leong, C. T. Jin, and A. McEwan, "Electrode contact impedance sensitivity to variations in geometry," *Physiol. Meas.*, vol. 33, no. 5, pp. 817–830, 2012.
- [13] V. Kolehmainen, M. Vauhkonen, P. A. Karjalainen, and J. P. Kaipio, "Assessment of errors in static electrical impedance tomography with adjacent and trigonometric current patterns," *Physiol. Meas.*, vol. 18, no. 4, pp. 289–303, 1997.
- [14] T. Vilhunen, J. P. Kaipio, P. J. Vauhkonen, T. Savolainen, and M. Vauhkonen, "Simultaneous reconstruction of electrode contact impedances and internal electrical properties: I. Theory," *Meas. Sci. Technol.*, vol. 13, no. 12, pp. 1848–1854, 2002.
- [15] L. M. Heikkinen, T. Vilhunen, R. M. West, and M. Vauhkonen, "Simultaneous reconstruction of electrode contact impedances and internal electrical properties: II. Laboratory experiments," *Meas. Sci. Technol.*, vol. 13, no. 12, pp. 1855–1861, 2002.
- [16] E. Demidenko, A. Borsic, Y. Wan, R. J. Halter, and A. Hartov, "Statistical estimation of EIT electrode contact impedance using a magic toeplitz matrix," *IEEE Trans. Biomed. Eng.*, vol. 58, no. 8, pp. 2194–2201, Aug. 2011.
- [17] H. Wu, Y. Yang, J. Escudero, and J. Jia, "Feasibility study of frequency-difference electrical impedance tomography on industrial applications," in *Proc. 8th World Congr. Ind. Process Tomogr.*, Iguassu Falls, Brazil, 2016, pp. 1–9.
- [18] R. Hayes, F. Podd, P. Newill, B. D. Grieve, and T. A. York, "Capacitively-coupled impedance measurements for ERT," in *Proc. 6th Int. Symp. Process Tomogr.*, Cape Town, South Africa, 2012, pp. 1–7.
- [19] M. Zhang and M. Soleimani, "Simultaneous reconstruction of permittivity and conductivity using multi-frequency admittance measurement in electrical capacitance tomography," *Meas. Sci. Technol.*, vol. 27, no. 2, p. 025405, 2016.
- [20] Z. Cao, L. Xu, C. Xu, and H. Wang, "Electrical resistance tomography (ERT) by using an ECT sensor," in *Proc. IST*, Thessaloniki, Greece, Jul. 2010, pp. 63–66.
- [21] B. L. Wang, Z. Y. Huang, H. F. Ji, and H. Q. Li, "Towards capacitively coupled electrical resistance tomography," in *Proc. WCIPT*, Beijing, China, 2010, pp. 1574–1577.
- [22] B. Wang, Y. Hu, H. Ji, Z. Huang, and H. Li, "A novel electrical resistance tomography system based on C4D technique," *IEEE Trans. Instrum. Meas.*, vol. 62, no. 5, pp. 1017–1024, May 2013.
- [23] B. Wang, W. Zhang, Z. Huang, H. Ji, and H. Li, "Modeling and optimal design of sensor for capacitively coupled electrical resistance tomography system," *Flow Meas. Instrum.*, vol. 31, pp. 3–9, Jun. 2013.
- [24] D. S. Holder, "Brief introduction to bioimpedance," in *Electrical Impedance Tomography: Methods, History and Applications*, 1st ed. London, U.K.: Inst. Phys. Publishing, 2005, pp. 416–418.
- [25] J. K. Seo, B. Harrach, and E. J. Woo, "Recent progress on frequency difference electrical impedance tomography," *ESAIM, Proc. EDP Sci.*, vol. 26, pp. 150–161, Apr. 2009.
- [26] J. K. Seo, J. Lee, S. W. Kim, H. Zribi, and E. J. Woo, "Frequency-difference electrical impedance tomography (fdEIT): Algorithm development and feasibility study," *Physiol. Meas.*, vol. 29, no. 8, pp. 929–944, Jul. 2008.
- [27] E. Malone, G. S. dos Santos, D. Holder, and S. Arridge, "Multifrequency electrical impedance tomography using spectral constraints," *IEEE Trans. Med. Imag.*, vol. 33, no. 2, pp. 340–350, Feb. 2014.
- [28] D. Watznig and C. Fox, "A review of statistical modelling and inference for electrical capacitance tomography," *Meas. Sci. Technol.*, vol. 20, no. 5, Apr. 2009, Art. no. 052002.
- [29] C. G. Xie *et al.*, "Electrical capacitance tomography for flow imaging: System model for development of image reconstruction algorithms and design of primary sensors," *IEE Proc. G-Circuits, Devices Syst.*, vol. 139, no. 1, pp. 89–98, Feb. 1992.

- [30] W. R. B. Lionheart, "EIT reconstruction algorithms: Pitfalls, challenges and recent developments," *Physiol. Meas.*, vol. 25, no. 1, pp. 125–142, Feb. 2004.
- [31] W. Q. Yang and L. Peng, "Image reconstruction algorithms for electrical capacitance tomography," *Meas. Sci. Technol.*, vol. 14, no. 1, p. R1, Jan. 2003.
- [32] Z. Cui *et al.*, "A review on image reconstruction algorithms for electrical capacitance/resistance tomography," *Sensor Rev.*, vol. 36, no. 4, pp. 429–445, Sep. 2016.
- [33] B. L. Su, Y. H. Zhang, L. H. Peng, D. Y. Yao, and B. F. Zhang, "The use of simultaneous iterative reconstruction technique for electrical capacitance tomography," *Chem. Eng. J.*, vol. 77, nos. 1–2, pp. 37–41, May 2000.
- [34] B. Wang, W. Tan, Z. Huang, H. Ji, and H. Li, "Image reconstruction algorithm for capacitively coupled electrical resistance tomography," *Flow Meas. Instrum.*, vol. 40, pp. 216–222, Dec. 2014.
- [35] L. Wang, X. Du, and X. Shao, "A hybrid ECT image reconstruction based on Tikhonov regularization theory and SIRT algorithm," *J. Phys., Conf. Ser.*, vol. 48, no. 1, pp. 1453–1458, 2007.
- [36] F. Mahmood, L.-G. Öfverstedt, M. Toots, G. Wilken, and U. Skoglund, "An extended field-based method for noise removal from electron tomographic reconstructions," *IEEE Access*, vol. 6, pp. 17326–17339, 2018, doi: [10.1109/ACCESS.2018.2810866](https://doi.org/10.1109/ACCESS.2018.2810866).
- [37] V. Sarode, S. Patkar, and A. N. Cheeran, "Comparison of 2-D algorithms in EIT based image reconstruction," *Int. J. Comput. Appl.*, vol. 69, no. 8, pp. 6–11, May 2013.
- [38] F. Mahmood, N. Shahid, U. Skoglund, and P. Vanderghyest, "Adaptive graph-based total variation for tomographic reconstructions," *IEEE Signal Process. Lett.*, vol. 25, no. 5, pp. 700–704, May 2018, doi: [10.1109/LSP.2018.2816582](https://doi.org/10.1109/LSP.2018.2816582).
- [39] F. Mahmood, N. Shahid, P. Vanderghyest, and U. Skoglund, "Graph-based sinogram denoising for tomographic reconstructions," in *Proc. IEEE EMBC*, Orlando, FL, USA, Aug. 2016, pp. 3664–3961.
- [40] S. Osher, M. Burger, D. Goldfarb, J. Xu, and W. Yin, "An iterative regularization method for total variation-based image restoration," *Multiscale Model. Simul.*, vol. 4, no. 2, pp. 460–489, 2005.
- [41] D. Silvera-Tawil, D. Rye, M. Soleimani, and M. Velonaki, "Electrical impedance tomography for artificial sensitive robotic skin: A review," *IEEE Sensors J.*, vol. 15, no. 4, pp. 2001–2016, Apr. 2015.
- [42] P. C. Hansen and D. P. O'Leary, "The use of the L-curve in the regularization of discrete ill-posed problems," *SIAM J. Sci. Comput.*, vol. 14, no. 6, pp. 1487–1503, Nov. 1993.
- [43] P. C. Hansen, "Analysis of discrete ill-posed problems by means of the L-curve," *SIAM Rev.*, vol. 34, no. 4, pp. 561–580, Dec. 1992.
- [44] E. Malone, G. S. D. Santos, D. Holder, and S. Arridge, "A reconstruction-classification method for multifrequency electrical impedance tomography," *IEEE Trans. Med. Imag.*, vol. 34, no. 7, pp. 1486–1497, Jul. 2015.
- [45] Y. Yang and J. Jia, "A multi-frequency electrical impedance tomography system for real-time 2D and 3D imaging," *Rev. Sci. Instrum.*, vol. 88, no. 8, Aug. 2017, Art. no. 085110.
- [46] R. J. Yerworth, R. H. Bayford, B. Brown, P. Milnes, M. Conway, and D. S. Holder, "Electrical impedance tomography spectroscopy (EITS) for human head imaging," *Physiol. Meas.*, vol. 24, no. 2, pp. 477–489, Apr. 2003.



YANDAN JIANG was born in Jinhua, China, in 1992. She received the B.Sc. degree from the Zhejiang University of Technology, Hangzhou, China, in 2013. She is currently pursuing the Ph.D. degree with the College of Control Science and Engineering, Zhejiang University, Hangzhou. She is also a Visiting Ph.D. Student with the Department of Electronic and Electrical Engineering, University of Bath, Bath, U.K. Her current research interests include automation instrumentation, multiphase flow measurement, ultrasound-based and electrical-based sensors, and electrical tomography.



MANUCHEHR SOLEIMANI received the B.Sc. degree in electrical engineering, the M.Sc. degree in biomedical engineering, and the Ph.D. degree in inverse problems and electromagnetic tomography from The University of Manchester, Manchester, U.K., in 1996, 1999, and 2005, respectively. From 2005 to 2007, he was a Research Associate with the School of Materials, The University of Manchester. In 2007, he joined the Department of Electronic and Electrical Engineering, University of Bath, Bath, U.K., where he was a Research Associate and became a Lecturer in 2008, a Senior Lecturer in 2013, a Reader in 2015, and a Full Professor in 2016. In 2011, he founded the Engineering Tomography Laboratory, University of Bath, where he was involved in various areas of tomographic imaging. His current research interests include electrical and electromagnetic imaging, nonlinear inverse problems, volumetric image reconstruction in X-ray CT, and multi-modality imaging.

• • •